Chapter 24
Mineral Mapping with Airborne Hyperspectral Thermal Infrared Remote Sensing at Cuprite, Nevada, USA

Dean N. Riley and Christoph A. Hecker

Abstract This is a case example of mineral mapping of unaltered and altered rocks at the Cuprite mining district, southwestern Nevada using the Spatially Enhanced Broadband Array Spectrograph System (SEBASS), a thermal infrared hyperspectral sensor that collects radiance measurements in the mid-wave infrared and thermal infrared portions of the electromagnetic spectrum. Cuprite, Nevada has been a test bed for a variety of multispectral and hyperspectral sensors that have predominantly covered the visible through short-wave infrared portion of the electromagnetic spectrum. In 2008, 20 SEBASS flight lines were collected at an average altitude of 4,735 m yielding an average 3.35 m ground sample distance (GSD).

Rock forming and alteration minerals found in this mining district have reststrahlen features (emission minima due to fast changes in refractive index with wavelength) in the thermal infrared portion of the electromagnetic spectrum (7.5–13.5 μm). Mineral mapping with hyperspectral thermal infrared data provides unique and complementary information to visible-shortwave (0.4–2.5 μm) hyperspectral data. Mineral maps were produced using a spectral feature fitting algorithm with publicly available mineral spectral libraries containing signatures.

These mineral maps were compared to the geological and alteration maps along with mineral maps generated by previous studies of visible-shortwave infrared hyperspectral sensors to assess some of the difference in mineral mapping with a hyperspectral thermal infrared sensor. This study shows that hyperspectral thermal infrared data can spectrally map rock forming minerals associated with unaltered rocks and alteration minerals associated with different phases of alteration in altered rocks at Cuprite, Nevada.

D.N. Riley (✉)
The Aerospace Corporation, Chantilly, VA, USA

SpecTIR, LLC, Fairfax, VA, USA
e-mail: Driley@spectir.com

C.A. Hecker
Faculty of Geo-Information Science and Earth Observation (ITC),
University of Twente, Enschede, The Netherlands

24.1   Introduction

Thermal spectroscopy of rocks and minerals has been of interest to the geological community and in its infancy was assisted by Kennecott Mining, and NASA (Lyon et al. 1959; Lyon and Burns 1963). The Air Force Research Lab and the USGS continued to support the early work of Lyon, Hunt, Salisbury, Vincent and others (Lyon and Burns 1963; Lyon 1965; Hunt 1970; Hunt and Salisbury 1974, 1976; Vincent et al. 1975) and show that the silicate and carbonate minerals have reflectance features from 8.0 to 14.0 microns (μm). These minerals are the primary rock forming minerals for almost every type of igneous, sedimentary, and metamorphic rock. Since this early work, these researchers and their students developed many of the techniques originally used in the multispectral remote sensing community. Work in the Long-wave Infrared (LWIR) did not stop after this early work.

NASA and the USGS conducted numerous field studies in the late 1970s and 1980s to develop and characterize multispectral airborne sensors (TIMS (Thermal Infrared Multispectral Scanner), GER-D (Kahle et al. 1980; Kahle 1987)). Continuation of the work led to the development of DAIS 7915, NASA's MASTER (MODIS-ASTER Airborne Simulator) airborne instrument and others (Hook et al. 2001; Mauger 2003; Müller et al. 2005). MASTER has 25 bands in the Midwave Infrared (MWIR, 3.0–5.5 μm) and LWIR in addition to 25 bands in the VNIR-SWIR (visible to short-wave infrared). Airborne LWIR (long-wave infrared) hyperspectral sensors were first built in the 1990s that included the MIRACO$_2$LAS (midinfrared airborne CO_2 laser system), SEBASS, AHI (Airborne Hyperspectral Imager), and ARGUS sensors (Whitbourn et al. 1990; Hackwell et al. 1996; Lucey et al. 1998; Cudahy et al. 1999). MIRACO$_2$LAS and ARGUS are line profiling instruments; whereas, SEBASS and AHI are airborne imaging instruments. ITRES of Canada (Pignatti et al. 2011) has started to sell and fly its 32 channel LWIR imager (TASI, Thermal Airborne Spectrographic Imager) and Specim of Finland (Holma et al. 2009, 2011) has begun production of its 84 channel LWIR imager (OWL). Moreover, The Aerospace Corporation (Aerospace) has built and flown new sensor designs, a 32-channel LWIR imager, MAGI (Mineral and Gas Identifier) (Hall et al. 2008), and a 128-channel LWIR imager, MAKO (Hall et al. 2011), using Dyson spectrometers, and NASA Jet Propulsion Laboratory (JPL) just recently flew HyTES (Hyperspectral Thermal Emission Spectrometer) in late 2012 (Hook 2012, personal communication). There has been a continued maturation of LWIR instruments from research and development prototypes towards production and this will increase the amount of TIR data that is available for exploitation.

Cuprite Hills of Nevada, USA has been imaged with a variety of airborne and spaceborne multispectral and hyperspectral instruments (ATM (Technology Microwave Sounder), AIS (AirborneImaging Spectrometer), TIMS, Geoscan, AVIRIS (Airborne Visible/Infrared Imaging Spectrometer), AISA (Airborne Hyperspectral Imaging Systems), CASI (Compact Airborne Spectral Imager), HYDICE (HYperspectral Digital Imagery Collection Experiment), MASTER, Landsat, Hyperion, ASTER (Advanced Spaceborne Thermal Emission and Reflection

Table 24.1 Flight log of SEBASS collection over Cuprite, Nevada

Session	Target X time (GMT)	Target name	Platform HAE (m) WGS84	Frames	IFOV (mrad)
080614_122714	12:32:12	CPRT4m_02	4738.88	3,500	1,100
080614_123753	12:42:19	CPRT4m_01	4717.83	3,500	1,100
080614_124749	12:52:42	CPRT4m_03	4725.82	3,500	1,100
080614_125914	13:03:02	CPRT4m_04	4749.33	3,500	1,100
080614_130855	13:13:31	CPRT4m_05	4717.25	3,500	1,100
080614_131925	13:23:56	CPRT4m_06	4732.5	3,500	1,100
080614_132934	13:34:21	CPRT4m_07	4732.18	3,500	1,100
080614_134040	13:44:53	CPRT4m_08	4740.28	3,500	1,100
080614_135032	13:55:14	CPRT4m_09	4731.83	3,500	1,100
080614_140047	14:05:12	CPRT4m_10	4753.42	3,500	1,100
080614_141108	14:15:26	CPRT4m_11	4746.1	3,500	1,100
080614_142046	14:25:41	CPRT4m_12	4731.78	3,500	1,100
080614_143111	14:35:36	CPRT4m_13	4731.21	3,500	1,100
080614_144104	14:45:30	CPRT4m_14	4730.06	3,500	1,100
080614_145038	14:55:16	CPRT4m_15	4721.26	3,500	1,100
080614_150031	15:05:12	CPRT4m_16	4733.35	3,500	1,100
080614_151028	15:14:40	CPRT4m_17	4732.91	3,500	1,100
080614_152001	15:24:27	CPRT4m_18	4753.63	3,500	1,100
080614_153016	15:34:33	CPRT4m_19	4743.58	3,500	1,100
080614_153943	15:44:08	CPRT4m_20	4747.14	3,500	1,100

Radiometer), and SEBASS) (Abrams et al. 1977; Ashley and Abrams 1980; Kahle and Goetz 1983; Kruse and Taranik 1989; Swayze et al. 1992; Mumin et al. 1996; Clark et al. 2003; Rowan et al. 2003; Allibone et al. 2004; Benavides et al. 2008a, b; Hecker 2012). The focus of this chapter is a case study demonstrating mineral mapping of rock forming and alteration minerals using airborne emittance spectroscopy over a site that has been consistently tested with visible to short-wave infrared (VNIR-SWIR) hyperspectral airborne and spaceborne sensors. Results from this study can be compared with the results from lower spectral resolution systems and lower signal to noise airborne sensors such as Aerospace's Mineral and Gas Identifier (MAGI), NASA JPL's MODIS/ASTER Airborne Simulator (MASTER), ITRES's TASI, or Specim's OWL sensors or current spaceborne sensors such as the Advanced Spaceborne Reflection and Emission Radiometer (ASTER) or NASA's proposed HYSPIRI sensor. Twenty SEBASS flight lines were flown and radiance data was recorded from 3.0 to 5.5 μm and 7.7 to 13.5 μm on June 14th, 2008 with a 3.35 meter (m) spatial resolution (Table 24.1).

24.2 Geologic Setting

In the southwestern part of the Great Basin in the United States south of the town of Goldfield, Nevada are the Cuprite Hills. These hills have limited vegetation cover and range from 1,400 to 1,700 m above sea level. Topographic relief in the western

part of the hills is controlled by a north trending ridge and circular hills in the eastern part of the hills. This area has moderately easy access as U.S. Highway 95 runs through the area (Ashley and Abrams 1980) (Fig. 24.1).

In the Cuprite Hills, the oldest rocks are found in the western section and are Cambrian in age. These are the Harkless, Mule Spring, and Emigrant Formations. The Harkless Formation (Єh) the oldest sequence in the area and is composed of siltstone, quartizitic siltstone, and orthoquartzite sandstone. Minerals present in these rocks are commonly chlorite, muscovite, biotite, and quartz. This is overlain by the Mule Spring Formation (Єms) which is a thin-bedded limestone that is finely crystalline. The primary mineral present in this formation is calcite. Overlying the Mule Spring Formation is the Emigrant Formation (Єe) which has limited outcrops and consists primarily of limestone and chert (Albers and Stewart 1972; Ashley and Abrams 1980) (Fig. 24.1).

Unconformably overlaying the Cambrian rocks are a series of Tertiary volcanic and sedimentary lithologies. The oldest Tertiary rocks are a rhyolite (Ts) that is observed in the eastern and western sections of the area and a quartz latite tuff, which is found in the western section. Minerals present are sanidine, quartz, plagioclase, and biotite. Plagioclase is absent in the quartz latite dike and biotite is limited. In the eastern section, there are exposures of porphyritic plagioclase olivine basalt that overlie the rhyolitic rocks (Ts). The minerals in this basalt (Tb1) are olivine and calcic-rich plagioclase. The basalt is overlain by the Stonewall Flat Tuff (Tsf) that consists of devitrified sodic rhyolitic ash-flow tuffs and some quartz latite dikes. Minerals present in this formation are sanidine, quartz, plagioclase and biotite. Whereas, the quartz latite dike in this formation has quartz, sanidine, and biotite phenocrysts. Lastly, the Pediment basalt (Tb2), in the western section, is a olivine-rich basalt and is the youngest of the Tertiary rocks with olivine and plagioclase as the primary minerals (Ashley and Abrams 1980) (Fig. 24.1).

The youngest rocks in the area are, Quaternary sand and gravel deposits (Qal) and Quaternary playa that overlay the Tertiary age rocks unconformably (Ashley and Abrams 1980) (Fig. 24.1).

24.2.1 Hydrothermal Alteration

Silicic, Opaline, and Argillic hydrothermal alteration were mapped in the area using traditional geological alteration mapping methods (Fig. 24.2). Silicic alteration is most prevalent in the eastern section of the area, but the areal extent is less than present in the western section. Hydrothermal quartz is the dominant mineral with minor kaolinite, alunite, and calcite (Ashley and Abrams 1980).

The most prevalent alteration is opalization. Opal, alunite, and kaolinite are the dominant minerals associated with this alteration. To a lesser degree, dickite, pyrophyllite, calcite, buddingtonite, muscovite, montmorillonite, and jarosite are observed in these rocks (Ashley and Abrams 1980; Swayze et al. 1992; Swayze 1997) (Fig. 24.2).
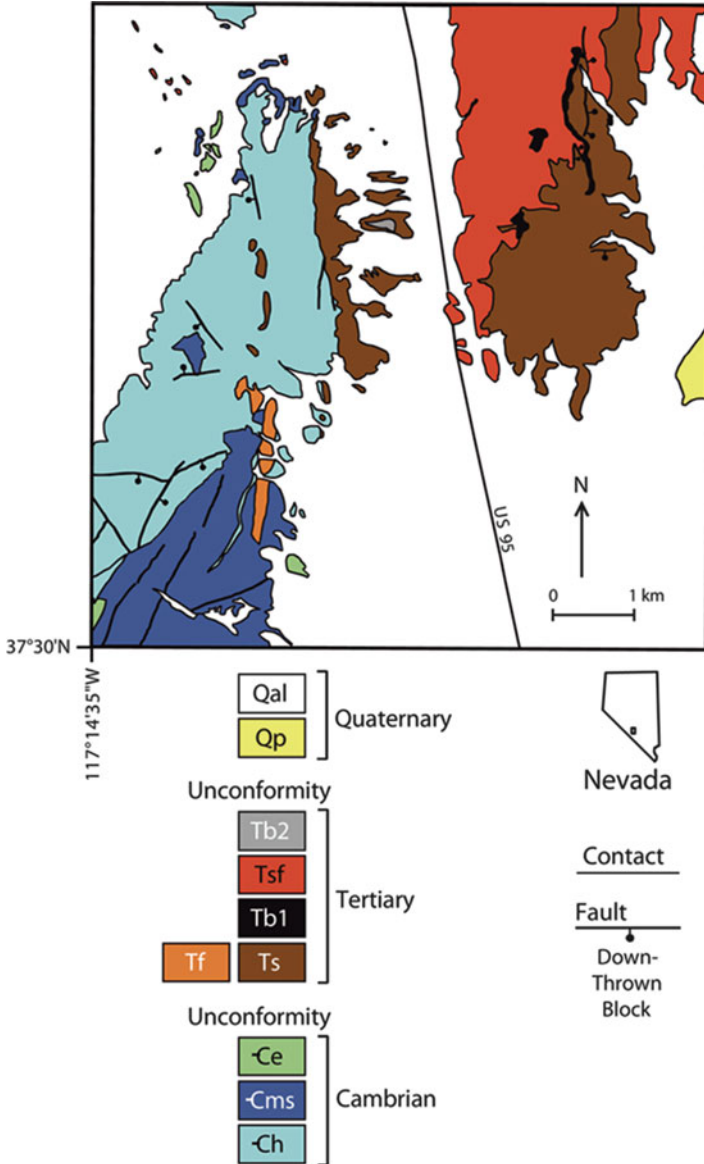
Fig. 24.1 Generalized geologic map of Cuprite mining district, Nevada (Rowan et al. 2003). *Qal* sand, gravel, and boulders, *Qp* playa deposits, *Tb2* olivine basalt, *Tsf* sodic ash-flow tuff, *Tb1* porphyritic olivine basalt, *Ts* crystal-rich rhyolite and latite tuff, conglomerate, and sandstone, *Tf* quartz latitic felsites, *Ce* limestone and chert, *Cms* limestone and lower limey siltstone, *Ch* phyllitic siltstone and minor sandy limestone (Modified from Ashley and Abrams 1980; Swayze 1997); *inset* map shows location of area in western Nevada
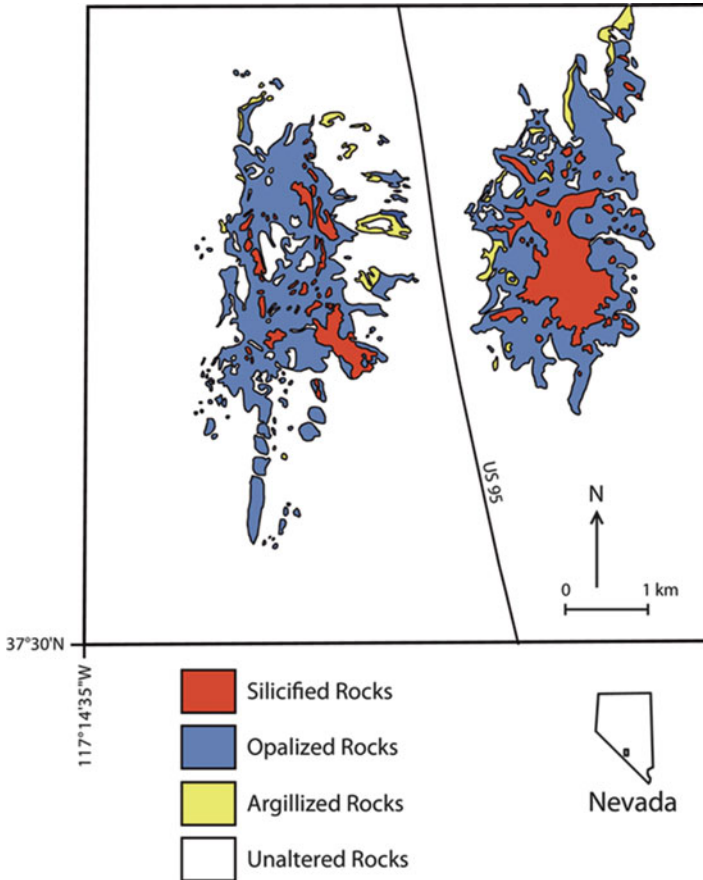
Fig. 24.2 Generalized map showing the distribution of three hydrothermally altered rock units: (1) *red*, silicified; (2) *blue*, opalized; and (3) *yellow*, argillized (Rowan et al. 2003) (Modified from Ashley and Abrams 1980)

Argillic alteration is the least intense and prevalent alteration style in the district. Recognition of this alteration is observed by plagioclase altering to kaolinite, bleaching of biotite, and volcanic glass altering to opal, montmorillonite, and kaolinite with quartz and sanidine remaining unaltered (Ashley and Abrams 1980) (Fig. 24.2).

24.3   Emittance of Minerals at Cuprite

Rock forming minerals have spectral features in the Thermal Infrared (TIR) region of the electromagnetic spectrum (5–25 μm). Fundamental vibrational frequencies of silicates, carbonates, sulfates, and phosphates show spectral features

in the 8–14 μm portion. Mineral identification is feasible because the spectral features (reststrahlen bands, i.e., emission minima due to fast changes in refractive index with wavelength) are diagnostic and display variations in wavelength position due to cation substitution (Salisbury et al. 1991; Hapke 1993).

Rocks and minerals have been measured in the laboratory using TIR spectroscopy and are used for mapping and identification of surface materials (Lyon et al. 1959; Lyon 1965; Farmer 1974; Salisbury et al. 1991; Christensen et al. 2000). Spectral libraries are readily available for mapping with airborne and spaceborne multispectral and hyperspectral data that contain spectra from 5 to 45 μm. The United States Geological Survey (USGS), NASA's Jet Propulsion Laboratory (JPL), Johns Hopkins University (JHU), Arizona State University (ASU) all have developed spectral libraries and are available online. NASA's ASTER spectral library is available online and is a compilation of the JPL's, JHU's, and the USGS's spectral libraries (Clark et al. 2007).

1. ASU spectral library (URL1)
2. ASTER spectral library (URL2)
3. USGS spectral library (URL3)

TIR spectra measured in hemispherical reflectance can be used to calculate emissivity using Kirchhoff's law. Emissivity (ε) is related to hemispherical reflectance (ρ) with the following equation (Salisbury et al. 1994).

This allows the use of rock and mineral spectral libraries collected in hemispherical reflectance to be used for spectral mapping of TIR data that has been converted to emissivity.

Mineral groups that have been mapped using multispectral TIR remote sensing data include silicates, carbonates, sulfates, phosphate, and clays (Kahle and Rowan 1980; Kahle and Goetz 1983; Gillespie et al. 1984; Kahle et al. 1988; Sabine et al. 1994; Crowley and Hook 1996; Hook et al. 1999; Rowan and Mars 2003). The use of hyperspectral TIR data for mineral mapping has received considerably less attention; however, silicates, carbonates, sulfates, and clays have been mapped (Cudahy et al. 2000; Hewson et al. 2000; Calvin et al. 2001; Vaughan et al. 2003, 2005; Vaughan and Calvin 2005; Riley et al. 2007, 2008; Aslett et al. 2008). In previous hyperspectral TIR studies a single flight line was flown over interesting geological features. This study involves mineral mapping of unaltered and altered rocks at Cuprite, across several parallel flightlines.

24.3.1 Unaltered Rocks

The Harkless Formation is made up of chlorite, muscovite, biotite, and quartz (Ashley and Abrams 1980). Chlorite has three reststrahlen bands in the 8–12 μm region, a deep one at 9.75 μm and two shallower features at 9.35 and 10.4 μm. Muscovite has reststrahlen features at 9.25 and 9.4 μm. The reststrahlen features of biotite are 9.2 and 9.8 μm. Quartz has two doublet reststrahlen features, one centered at 8.65 μm with minima at 8.5 and 8.9 μm and the other at 12.6 μm with

Fig. 24.3 *Upper plot*:
Thermal spectral signatures
of chalcedony (*blue*, *upper*),
quartz (*green*, *middle*), calcite
(*red*, *lower*). *Lower plot*:
Thermal spectral signatures
of opal (*blue*, *upper*),
kaolinite (*green*, *middle*),
alunite (*red*, *lower*)
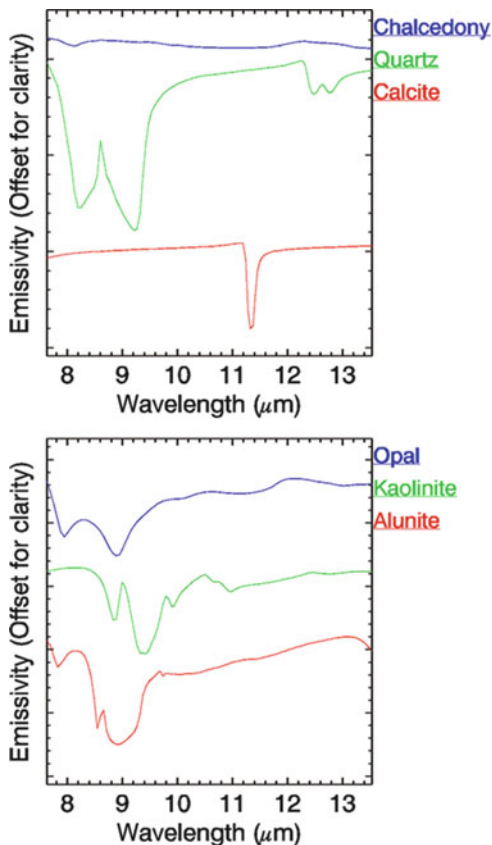
minima at 12.5 and 12.8 μm. Whereas, the Mule Spring Formation is limestone and
its primary mineral is calcite which has a reststrahlen feature at 11.3 μm (Figs. 24.3
and 24.4).

Rhyolite (Ts) is composed of quartz, sanidine, plagioclase, and biotite
phenocrysts. The quartz latite tuff (Tf) consists of predominantly quartz and
alkali-feldspar (sanidine) with scarce biotite phenocrysts. The Stonewall Flat Tuff
(Tsf) is composed of devitrified sodic rhyolite ash-flow tuffs and a quartz latite dike.
These rocks have sanidine phenocrysts with quartz and sodic feldspar groundmass
(Ashley and Abrams 1980). Plagioclase in silicic volcanic rocks is commonly
albite, oligoclase or even andesine. Reststrahlen bands for sanidine are at 8.65
and 9.5 μm and biotite has bands at 9.2 and 9.8 μm. Albite has multiple reststrahlen
features at 8.7, 9.2, 9.6, and 9.9 μm. Oligoclase has reststrahlen bands at 8.7 and
9.9 μm and andesine has bands at 8.8 and 9.9 μm. As the calcic content of
plagioclase increases from albite to andesine there is a shift to longer wavelength
from 8.7 to 9.0 μm reststrahlen band. The reststrahlen bands for plagioclase shift
from anorthite to albite (Cudahy et al. 2000) (Figs. 24.3 and 24.4).

Fig. 24.4 *Upper plot*:
Thermal spectral signatures
of muscovite (*blue*, *upper*),
chlorite (*green*, *middle*),
biotite (*red*, *lower*). *Lower
plot*: Thermal spectral
signatures of andesine (*dark
green*, *upper*), Oligoclase
(*dark red*, *upper-middle*),
albite (*blue*, *middle*),
orthoclase (*green*, *lower-
middle*), sanidine (*red*, *lower*)
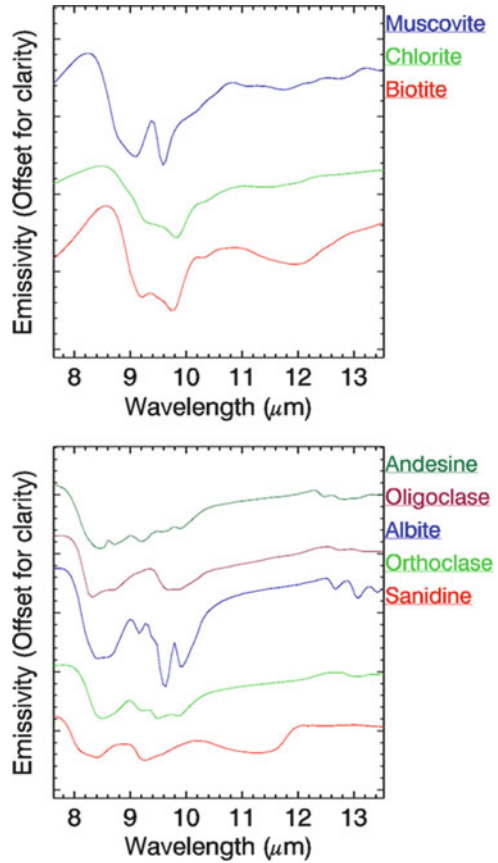
24.3.2 Altered Rocks

Silicic alteration is more prevalent in eastern section of area, but the areal extent is less
in the western section. Hydrothermal quartz is the dominant mineral with minor
kaolinite, alunite, and calcite (Ashley and Abrams 1980). Hydrothermal quartz has a
doublet of reststrahlen features with a peak in between centered at 8.65 μm and the
features at 8.5 and 8.9 μm. Kaolinite has multiple reststrahlen features at 8.9, 9.6, 9.9,
and 11.0 μm with the features at 9.6 and 11.0 being the most significant. Alunite has an
asymmetric doublet with a peak at 8.7 μm and the features at 8.4 and 9.0 μm (Figs. 24.3
and 24.4). An asymmetric doublet that is slightly different than pure quartz has been
noted (Vaughan et al. 2003). Moreover, chalcedony has an asymmetric doublet that is
similar to the quartz-alunite combined signature. As noted by (Vaughan et al. 2003),
these spectral similarities make separating quartz, alunite, quartz-alunite, chalcedony,
and opal in the TIR difficult (Figs. 24.3 and 24.4), but feasible.

Opalized alteration is the most prevalent alteration present. Opal, alunite, and kaolinite are the dominant minerals associated with this alteration. Dickite, pyrophyllite, calcite, buddingtonite, muscovite, montmorillonite, and jarosite can be observed in these rocks as well (Ashley and Abrams 1980; Swayze et al. 1992; Swayze 1997). Opal has a single reststrahlen feature at 8.8 μm. Alunite has reststrahlen bands at 8.4 and 9.0 μm with a peak in between at 8.7 μm. Kaolinite's multiple reststrahlen bands are at 8.9, 9.6, 9.9, and 11.0 μm (Figs. 24.3 and 24.4). Calcite has a reststrahlen band at 11.3 μm and muscovite has features at 9.25 and 9.4 μm. The reststrahlen features of dickite, pyrophyillite, buddingtonite, montmorillonite, and jarosite will not be discussed as these minerals will not be mapped for brevity (Figs. 24.3 and 24.4).

The areal extent of argillic alteration in the district is the least intense and prevalent. This alteration is recognized by plagioclase altering to kaolinite, bleaching of biotite, and volcanic glass altering to opal, montmorillonite, and kaolinite. Quartz and sanidine are unaltered (Figs. 24.3 and 24.4).

24.4 SEBASS Analysis

24.4.1 Data Collection and Calibration

Spatially Enhanced Broadband Array Spectrograph System (SEBASS) measures reflected and emitted radiation with 128 channels from 2.5 to 5.3 μm and measures emitted radiation with 128 channels from 7.6 to 13.5 μm of the electromagnetic spectrum. This instrument operates as a pushbroom sensor with 128 pixels in the cross-track direction and has a 7.8° FOV and 1.1-mrad IFOV per pixel. A flight altitude of approximately 3,000 m above ground level (AGL) producing a 3.35-m resolution was flown for this study. When flown with greater area coverage, the signal-to-noise (SNR) ratio has been tested greater than 2,000:1 (Hackwell et al. 1996).

Under clear sky conditions, SEBASS data were collected over Cuprite, Nevada in June, 2008. Following the steps outlined by Hackwell et al. (1996), these data were calibrated to at-sensor radiance. Especially important was the use of cold and hot blackbodies at the beginning and end of each flight line for in flight calibration. These data were preprocessed for striping prior to atmospheric compensation and masking of bad pixels (Dykstra and Segal 1985). At surface radiance data were produced using an In Scene Atmospheric Correction (ISAC) algorithm (Young et al. 2002). These data were converted to apparent emissivity and temperature using a Emissivity Normalization Method (ENM) for the temperature emissivity separation (TεS) (Gillespie 1986; Kealy and Hook 1993). The emissivity data were smoothed using a Savitzky-Golay filter prior to spectral mapping (Savitzky and Golay 1964; Tsai and Philpot 1998; King et al. 1999; Ruffin and King 1999). Lastly, these LWIR data were subset from 8.0 to 12.0 μm prior to spectral feature

absorption mapping because most of minerals at Cuprite have absorption features constrained to this region.

24.4.2 Image Analysis

Figure 24.5 shows a false color composite image and a decorrelation image of SEBASS's channels at 11.09, 9.60, and 9.02 μm displayed as red, green, and blue (Gillespie et al. 1986). Vaughan et al. (2003) noted that quartz dominated regions should appear yellow, clay-rich areas are magenta, quartz-sulfate mixtures are a green, and quartz-feldspar-clay mixtures are orange-brown in color. At Cuprite using similar wavelengths, the Harkless Formation appears as red which primarily composed of chlorite, muscovite, biotite, and quartz. Whereas, the Mule Spring Formation appear as blue (calcite-rich) and the Stonewall Flat Formation appears as blue with a lot of orange-brown (quartz- and feldspar-rich). The alteration centers appear as green with yellow and they are dominated with quartz-alunite mixtures; while, the orange-brown areas are quartz, feldspar, and clay rich.

24.4.3 Spectral Feature Processing

Spectral mapping of the minerals was conducted using spectral feature fitting in ENVI with a spectral library constrained to the probable minerals at Cuprite which is similar to the methods developed by (Clark and Roush 1984; Swayze 1997; Clark et al. 2003). ENVI's spectral feature fitting routine produces a scaled image and a root mean square (RMS) image for each spectral signature mapped using a least squares routine and a "fit image" can be generated by dividing the scaled image with the rms image. A threshold of two standard deviations was applied to the fit image.

Alunite is spectrally mapped in the western section moderately well when compared to VNIR-SWIR spectral mapping of Clark et al. (2003). Spatially there is less alunite mapped in eastern alteration location. In both cases, alunite is spectrally mapped as a bulls-eye pattern around the silicified alteration. The alluvium is mapping some alunite which is probably from the weathering of the rocks.

Spectral mapping of chlorite is predominantly in the Harkless Formation (Ꞓh), western section of Fig. 24.7. Chlorite is seen in the alluvium as well and is most likely from the weathering of the Harkless Formation. The Stonewall Flat Tuff (Tsf) also has some chlorite spectrally mapping on it. The weathering of biotite to chlorite is most likely the result of this spectral mapping.

In the eastern alteration center, the spectral mapping of quartz is coherent and overlies the silicified alteration described by Ashley and Abrams (1980). Quartz also maps well the smaller silicified alteration observed in the western alteration
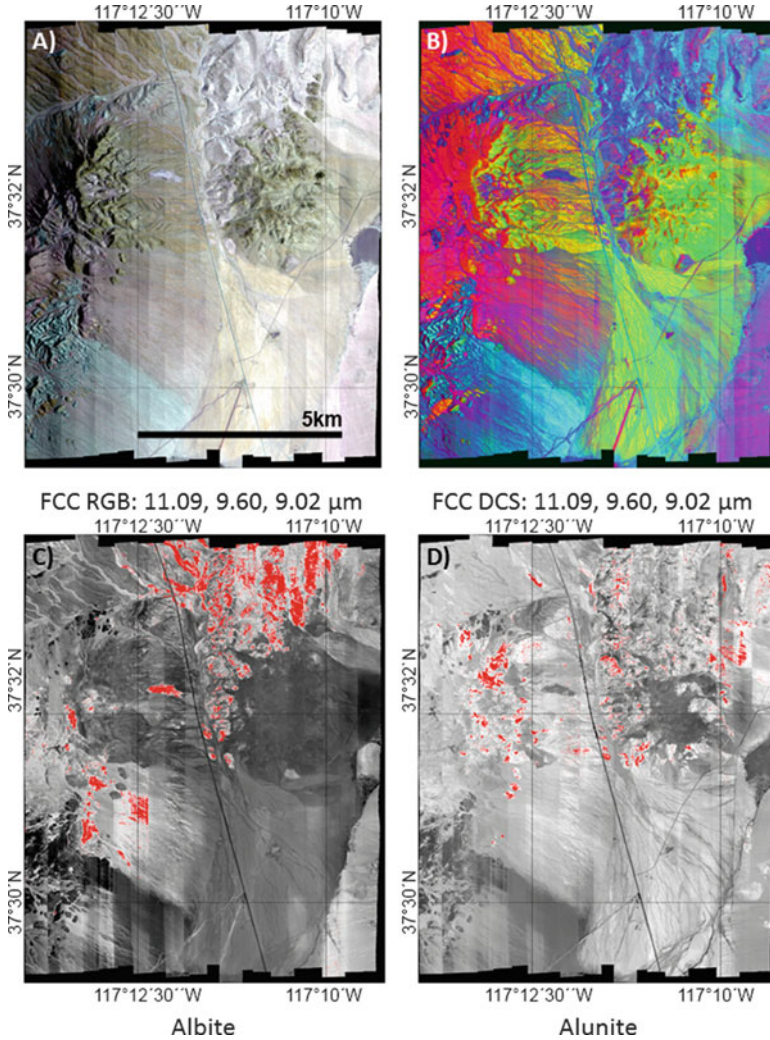
Fig. 24.5 *Upper left*: Mosaicked false color composite (*FCC*) image at R: 11.09, G: 9.60, and B: 9.02 μm. *Upper right*: Mosaicked decorrelation stretch false color composite (*FCC-DCS*) image at R: 11.09, G: 9.60, and B: 9.02 μm. *Lower left*: Mosaicked albite gray scale image from least squares material matching algorithm overlain with threshold at 2 standard deviations. *Lower right*: Mosaicked alunite gray scale image from least squares material matching algorithm overlain with threshold at 2 standard deviations

center. The rhyolitic tuffs and quartz latite is spectrally mapped well in the northwestern section (Fig. 24.8).

Calcite is spectrally mapped in the southwestern portion of the figure and correlates well with the Mule Spring Formation. Calcite is also mapped spectrally in smaller outcrops in the northwest and in the southeast. U.S Highway 95 is also
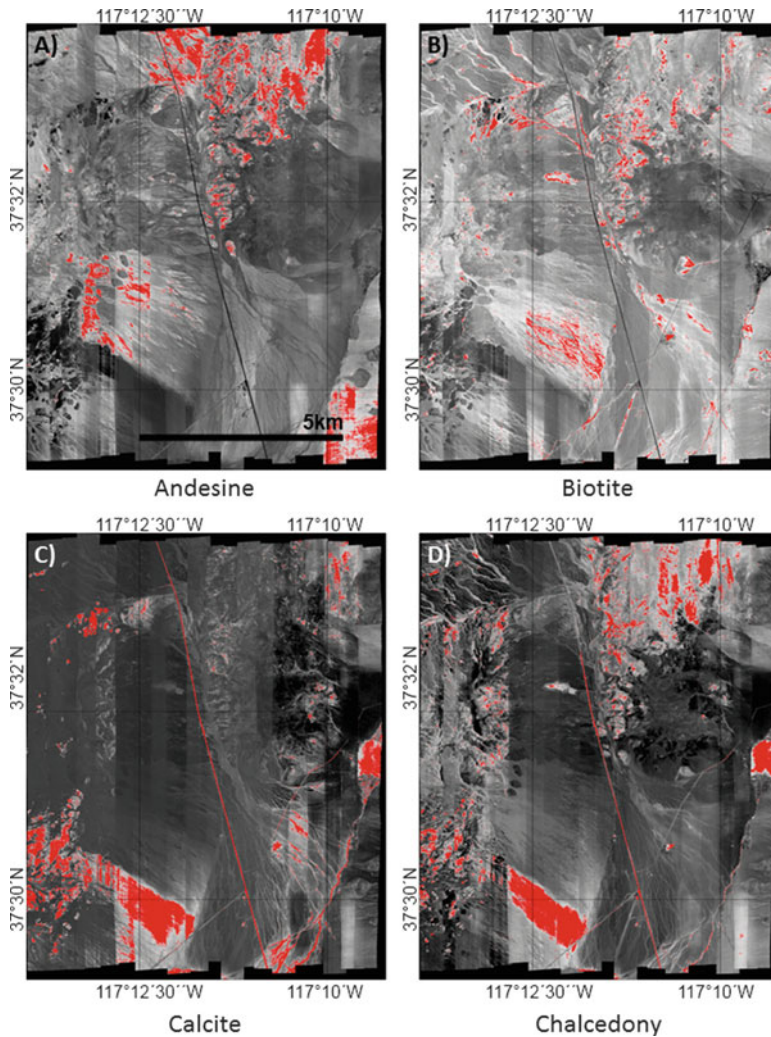
Fig. 24.6 *Upper left*: Mosaicked andesine gray scale image from least squares material matching algorithm overlain with threshold at 2 standard deviations. *Upper right*: Mosaicked biotite gray scale image from least squares material matching algorithm overlain with threshold at 2 standard deviations. *Lower left*: Mosaicked calcite gray scale image from least squares material matching algorithm overlain with threshold at 2 standard deviations. *Lower right*: Mosaicked chalcedony gray scale image from least squares material matching algorithm overlain with threshold at 2 standard deviations

mapped with calcite which is not surprising since asphalt commonly has calcite in it (Fig. 24.6).

Chalcedony is spectrally mapped in the western alteration center overlying the silicified alteration zone. It is also mapped in the Stonewall Flat Tuff (Tsf) and over
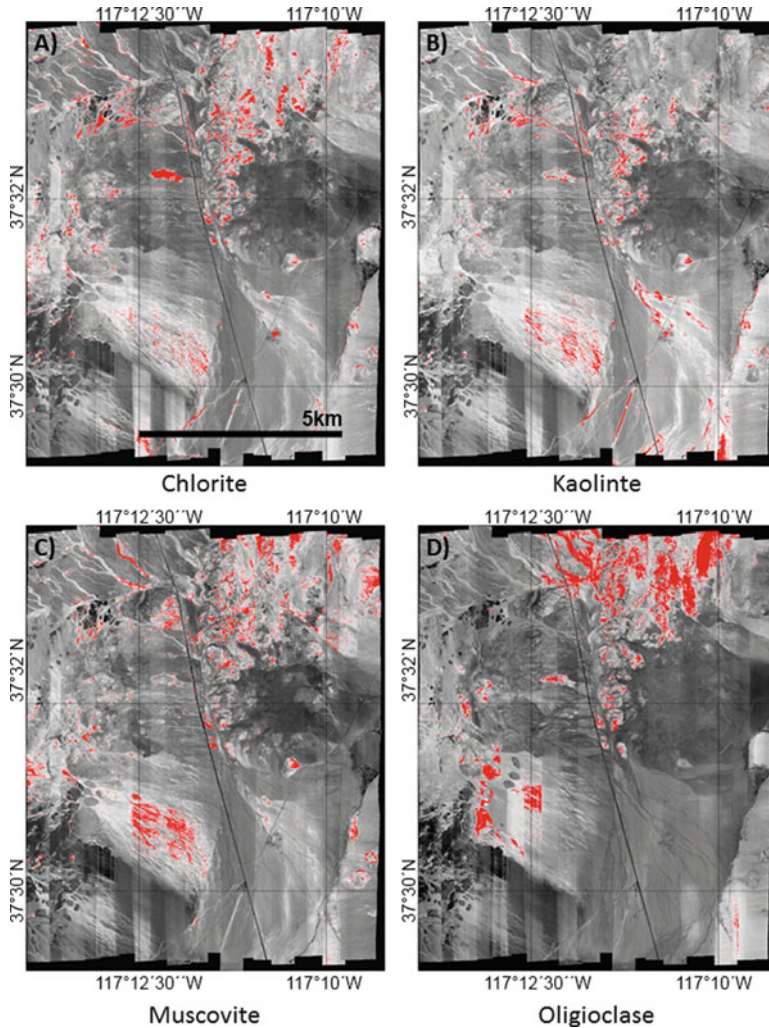
Fig. 24.7 *Upper left*: Mosaicked chlorite gray scale image from least squares material matching algorithm overlain with threshold at 2 standard deviations. *Upper right*: Mosaicked kaolinite gray scale image from least squares material matching algorithm overlain with threshold at 2 standard deviations. *Lower left*: Mosaicked muscovite gray scale image from least squares material matching algorithm overlain with threshold at 2 standard deviations. *Lower right*: Mosaicked oligoclase gray scale image from least squares material matching algorithm overlain with threshold at 2 standard deviations

parts of the Mule Spring Formation (Ꞓms). The spatial coherency of chalcedony is less than quartz spectral mapping over the silicified alteration center (Fig. 24.6).

Spectral mapping of muscovite occurs over the Harkless Formation in the western alteration area and in some of the argillic alteration area in the east alteration center (Fig. 24.7). This mapping in the eastern area is mainly located between the eastern alteration area and the Stonewall Flat Tuff (Tsf).
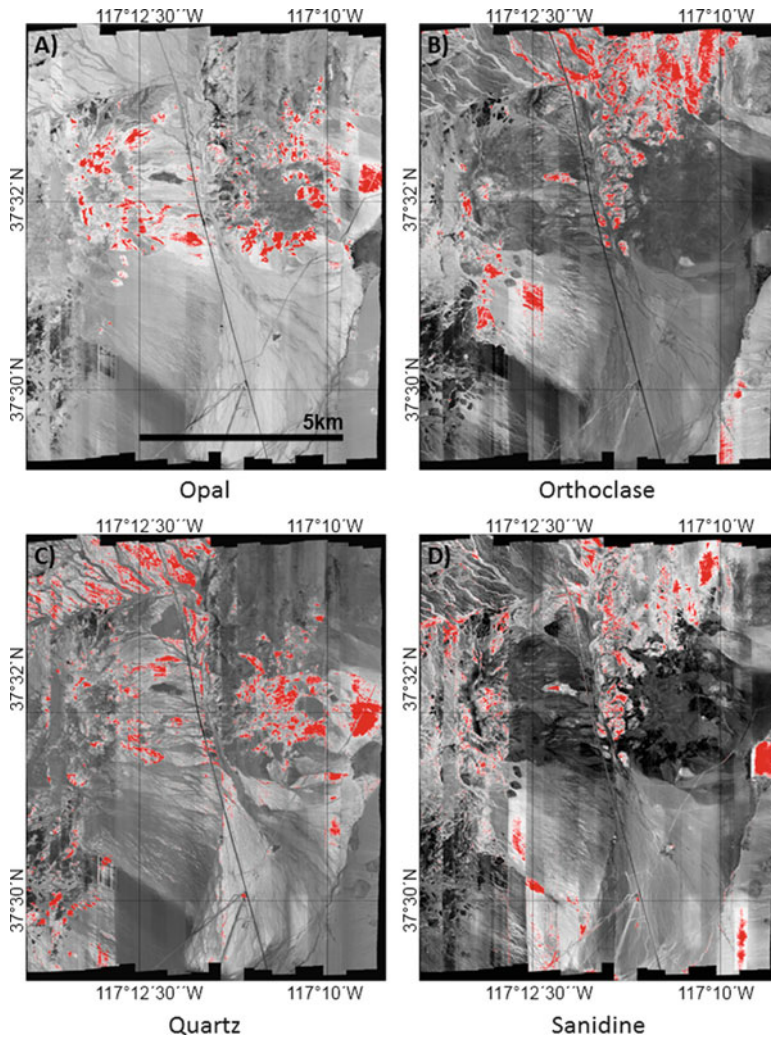
Fig. 24.8 *Upper left*: Mosaicked opal gray scale image from least squares material matching algorithm overlain with threshold at 2 standard deviations. *Upper right*: Mosaicked orthoclase gray scale image from least squares material matching algorithm overlain with threshold at 2 standard deviations. *Lower left*: Mosaicked quartz gray scale image from least squares material matching algorithm overlain with threshold at 2 standard deviations. *Lower right*: Mosaicked sanidine gray scale image from least squares material matching algorithm overlain with threshold at 2 standard deviations

Kaolinite spectrally maps mostly in the western alteration area and along the west and north of the eastern alteration area. Kaolinite is also found in the alluvium as well and maps around the Pediment basalt (Tb2) coherently (Fig. 24.7).

Opal is found from spectral mapping in the western alteration area and outside of the silicified alteration in the eastern alteration area. Opal is spectrally mapped in

the Stonewall Flat Tuff (Tsf) which is the result of weathering and devitrification of the rhyolites and quartz latite (Fig. 24.8).

Coherent patterns of alunite, calcite, chalcedony, chlorite, kaolinite, muscovite, opal, quartz, sanidine were mapped using a least-squares based spectral feature fitting algorithm applied to SEBASS apparent emissivity data. Rock forming minerals associated with unaltered rocks were mapped correlating with the Harkless, Mule Spring, and Stonewall Flat Tuff Formations. Alteration minerals associated with argillic, opalized, and silicified alteration were mapped and correlate with alteration map produced by (Ashley and Abrams 1980).

Mineral mapping of chlorite correlates with the Harkless formation. Some muscovite and quartz spectrally maps with the Harkless Formation as well. Calcite spectrally maps predominantly within the Mule Spring Formation in the southwestern section of the district.

Argillic alteration is limited, but kaolinite and muscovite both map outside of the opalized alteration in the eastern and western alteration centers.

Opalized alteration is predominantly in the eastern alteration center and is spectral mapped using an opal signature. Alunite was detected in the opalized alteration areas as well, while Chalcedony does not significantly overlap with opal.

Silicified alteration (represented by quartz spectral map) is dominantly detected in the eastern alteration center. Chalcedony maps in the silicified alteration as well, but this is more likely the result of minor alunite being present than chalcedony being present. This is similar to what was seen with other quartz-alunite rocks having a similar spectral signature to chalcedony (Vaughan et al. 2003). Separating different types of siliceous minerals is feasible even though the minerals have similar spectral shapes and absorption features.

24.5   Summary and Conclusions

Thermal infrared hyperspectral remote sensing at Cuprite, Nevada shows Stonewall Flat Tuff, rhyolite, and quartz-latite tuff can be spectrally mapped. This is in addition to the Harkless and Mule Spring Formations being spectrally mapped as well. The eastern and western alteration centers with their silicic, opaline, and argillic alteration are also mapped spectrally. These results indicate that rock forming and alteration minerals can be mapped with similar and complementary results to visible to short-wave infrared hyperspectral mineral mapping. Differentiating chlorite and calcite in the thermal infrared is much easier in the thermal infrared than in the short-wave infrared since the absorption features of these minerals do not overlap this portion of the electromagnetic spectrum. Moreover, mineral mapping techniques developed for the visible to short-wave infrared hyperspectral sensors are applicable in the thermal infrared once the data has been converted to emissivity.

References

Abrams MJ, Ashley RP, Rowan LC, Goetz AFH, Kahle AB (1977) Mapping of hydrothermal alteration in the Cuprite mining district, Nevada, using aircraft scanner images for the spectral region 0.46 to 2.36 μm. Geology 5(12):713–718

Albers JP, Stewart JH (1972) Geology and mineral deposits of Esmeralda County, Nevada. Nev Bur Mines Geol Bull 78:80

Allibone A, Hayden P, Cameron G, Duku F (2004) Paleoproterozoic gold deposits hosted by albite- and carbonate-altered tonalite in the Chirano District, Ghana, West Africa. Econ Geol 99:479–497

Ashley RP, Abrams MJ (1980) Alteration mapping using multispectral images – Cuprite mining district, Esmeralda County, Nevada. Open-File Report, United States Geological Survey, 17p, 14 plates, (some col.), maps; 28 cm

Aslett Z, Taranik JV, Riley DN (2008) Mapping rock-forming minerals at daylight pass, Death Valley National Park, California, using SEBASS thermal-infrared hyperspectral image data. In: Geoscience and remote sensing symposium, 2008. IGARSS 2008. IEEE International, Boston

Benavides J, Kyser TK, Clark AH, Stanley C, Oates C (2008a) Application of molar element ratio analysis of lag talus composite samples to the exploration for iron oxide–copper–gold mineralization: Mantoverde area, northern Chile. Geochem Explor Environ Anal 8(3–4):369–380

Benavides J, Kyser TK, Clark AH, Stanley C, Oates C (2008b) Exploration guidelines for copper-rich iron oxide–copper–gold deposits in the Mantoverde area, northern Chile: the integration of host-rock molar element ratios and oxygen isotope compositions. Geochem Explor Environ Anal 8(3–4):343–367

Calvin WM, Vaughan RG, Taranik JV, Smailbegovic A (2001) Mapping natural and human influenced acid sulfate weathering near Reno, NV using the SEBASS hyperspectral instrument. In: Geoscience and remote sensing symposium, 2001. IGARSS '01. IEEE 2001 International. Sidney NSW, Australia

Christensen PR, Bandfield JL, Hamilton VE, Howard DA, Lane MD, Piatek JL, Ruff SW, Stefanov WL (2000) A thermal emission spectral library of rock-forming minerals. J Geophys Res 105(E4):9735–9739

Clark RN, Roush TL (1984) Reflectance spectroscopy' quantitative analysis techniques for remote sensing applications. J Geophys Res 89(B7):6329–6340

Clark RN, Swayze GA, Livo KE, Kokaly RF, Sutley SJ, Dalton JB, McDougal RR, Gent CA (2003) Imaging spectroscopy: Earth and planetary remote sensing with the USGS Tetracorder and expert systems. J Geophys Res 108(E12):5131

Clark RN, Swayze GA, Wise R, Livo KE, Hoefen TM, Kokaly RF, Sutley SJ (2007) USGS digital spectral library splib06a, Digital data series 231. U.S. Geological Survey, Denver

Crowley JK, Hook SJ (1996) Mapping playa evaporite minerals and associated sediments in Death Valley, CA, with multispectral thermal infrared images. J Geophys Res 101(B1):643–660

Cudahy TJ, Whitbourn LB, Connor PM, Mason P, Phillips RN (1999) Mapping surface mineralogy and scattering behavior using backscattered reflectance from a hyperspectral midinfrared airborne CO2 laser system (MIRACO2LAS). IEEE Trans Geosci Remote Sens 37(4):2019–2034

Cudahy TJ, Okada K, Yamato Y, Maekawa M, Hackwell JA, Huntington JF (2000) Mapping skarn and porphyry alteration mineralogy at Yerington, Nevada, using airborne hyperspectral TIR

SEBASS data. CSIRO Exploration and Mining report 734R. CSIRO Exploration and Mining, Underwood Avenue, Floreat Park, WA, Australia, p 78

Dykstra JD, Segal DB (1985) Analysis of AIS data of the recluse oil field, Recluse, Wyoming. In: Proceedings AIS workshop. NASA Jet Propulsion Laboratory, Pasadena, CA

Farmer VC (1974) The infrared spectra of minerals. Mineralogical Society, London

Gillespie AR (1986) Lithologic mapping of silicate rocks using TIMS. The TIMS data users' workshop. NASA Jet Propulsion Laboratory, Pasadena

Gillespie AR, Kahle AB, Palluconi FD (1984) Mapping alluvial fans in Death Valley, CA using multispectral thermal infrared images. Geophys Res Lett 11:1153–1156

Gillespie AR, Kahle AB, Walker RE (1986) Color enhancement of highly correlated images. I. Decorrelation and HSI contrast stretches. Remote Sens Environ 20(3):209–235

Hackwell JA, Warren DW, Bongiovi RP, Hansel SJ, Hayhurst TL, Mabry DJ, Sivjee MG, Skinner JW (1996) LWIR/MWIR imaging hyperspectral sensor for airborne and ground-based remote sensing. SPIE, Denver

Hall JL, Hackwell JA, Tratt DM, Warren DW, Young SJ (2008) Space-based mineral and gas identification using a high-performance thermal infrared imaging spectrometer. SPIE, San Diego

Hall JL, Boucher RH, Gutierrez DJ, Hansel SJ, Kasper BP, Keim ER, Moreno NM, Polak ML, Sivjee MG, Tratt DM, Warren DW (2011) First flights of a new airborne thermal infrared imaging spectrometer with high area coverage. SPIE, Orlando

Hapke B (1993) Combined theory of reflectance and emittance spectroscopy. In: Pieters CM, Englert PAJ (eds) Topics in remote sensing 4-remote geochemical analysis: elemental and mineralogical composition. Cambridge University Press, Cambridge, pp 31–42

Hecker CA (2012) Mapping feldspars from above - a thermal infrared and partial least squares-based approach. Doctorate of Philosophy dissertation, University of Twente, Enschede

Hewson RD, Hausknecht P, Cudahy TJ, Huntington JF, Mason P, Hackwell JA, Nikitas J, Okada K (2000) An appraisal of the hyperspectral thermal-infrared SEBASS data recorded from Oatman, Arizona and a comparison of their unmixed results with AVIRIS. Exploration and Mining report 668 F. CSIRO Exploration and Mining, Wembley, Western Australia, p 38

Holma H, Hyvarinen T, Lehtomaa J, Karjalainen H, Jaskari R (2009) Advanced pushbroom hyperspectral LWIR imagers. SPIE, Orlando

Holma H, Mattila AJ, Hyvarinen T, Weatherbee O (2011) Advances in hyperspectral LWIR pushbroom imagers. SPIE, Orlando

Hook SJ, Abbott EA, Grove C, Kahle AB, Palluconi FD (1999) Use of multispectral thermal infrared data in geological studies. In: Rencz AN (ed) Remote sensing for the earth sciences. Wiley, New York, p 3

Hook SJ, Myers JJ, Thome KJ, Fitzgerald M, Kahle AB (2001) The MODIS/ASTER airborne simulator (MASTER) – a new instrument for earth science studies. Remote Sens Environ 76 (1):93–102

Hunt GR (1970) Visible and near-infrared spectra of minerals and rocks: I. Silicate minerals. Mod Geol 1:283–300

Hunt GR, Salisbury JW (1974) Mid-infrared spectral behavior of igneous rocks. Environmental research paper. U.S. Air Force Cambridge Research Laboratory, Cambridge

Hunt GR, Salisbury JW (1976) Mid-infrared spectral behavior of metamorphic rocks. Environmental research paper. U.S. Air Force Cambridge Research Laboratory, Cambridge

Kahle AB (1987) Surface emittance, temperature, and thermal inertia derived from Thermal Infrared Multispectral Scanner (TIMS) data for Death Valley, California. Geophysics 52 (7):858–874

Kahle AB, Goetz AFH (1983) Mineralogic information from a new airborne thermal infrared multispectral scanner. Science 222:24–27

Kahle AB, Rowan LC (1980) Evaluation of multispectral middle infrared aircraft images for lithologic mapping in the East Tintic Mountains, Utah. Geology 8:234–239

Kahle AB, Madura DP, Soha JM (1980) Middle infrared multispectral aircraft scanner data: analysis for geological applications. Appl Opt 19(14):2279–2290

Kahle AB, Gillespie AR, Abbott EA, Abrams MJ, Walker RE, Hoover G, Lockwood JP (1988) Relative dating of Hawaiian lavea flows using multispectral thermal infrared images: a new tool for geologic mapping of young volcanic terrains. J Geophys Res 93:15239–15251

Kealy PS, Hook SJ (1993) Separating temperature and emissivity in thermal infrared multispectral scanner data: implications for recovering land surface temperatures. IEEE Trans Geosci Remote Sens 31(6):1155–1164

King RL, Ruffin C, LaMastus FE, Shaw DR (1999) The analysis of hyperspectral data using Savitzky-Golay filtering-practical issues. 2. In: Geoscience and remote sensing symposium, 1999. IGARSS '99 Proceedings. IEEE 1999 International. Hamburg, Germany

Kruse FA, Taranik DL (1989) Mapping hydrothermally altered rocks with the airborne imaging spectrometer (AIS) and the airborne visible/infrared imaging spectrometer. In: Geoscience and remote sensing symposium, 1989. IGARSS'89. 12th Canadian symposium on remote sensing, 1989 International. Vancouver, Canada

Lucey PG, Williams TJ, Mignard M, Julian J, Kobubun D, Allen G, Hampton D, Schaff W, Schlangen MJ, Winter EM, Kendall WB, Stocker AD, Horton KA, Bowman AP (1998) AHI: an airborne long-wave infrared hyperspectral imager. SPIE, San Diego

Lyon RJP (1965) Analysis of rocks by spectral infrared emission (8 to 25 microns). Econ Geol 60 (4):715–736

Lyon RJP, Burns EA (1963) Analysis of rocks and minerals by reflected infrared radiation. Econ Geol 58(2):274–284

Lyon RJP, Tuddenham WM, Thompson CS (1959) Quantitative mineralogy in 30 minutes. Econ Geol 54(6):1047–1055

Mauger A (2003) Comparison of various remote sensing and spectral radiometer instruments. MESA J 29:26–29

Müller A, Richter R, Habermeyer M, Dech S, Segl K, Kaufmann H (2005) Spectroradiometric requirements for the reflective module of the airborne spectrometer ARES. IEEE Geosci Remote Sens Lett 2(3):329–332

Mumin AH, Fleet ME, Longstaffe FJ (1996) Evolution of hydrothermal fluids in the Ashanti gold belt, Ghana; stable isotope geochemistry of carbonates, graphite, and quartz. Econ Geol 91:135–148

Pignatti S, Lapenna V, Palombo A, Pascucci S, Pergola N, Cuomo V (2011) An advanced tool of the CNR IMAA EO facilities: overview of the TASI-600 hyperspectral thermal spectrometer. In: 3rd workshop on hyperspectral image and signal processing: evolution in remote sensing (WHISPERS), Lisbon, 6–9 June 2011. Lisbon, Portugal. doi:10.1109/WHISPERS.2011.6080890

Riley DN, Cudahy TJ, Hewson RD, Jansing D, Hackwell JA (2007) SEBASS imaging for copper porphyry and skarn deposits, Yerington, NV. In: Proceedings of exploration 07: fifth decennial international conference on mineral exploration, Toronto, Canada

Riley DN, Mars JC, Cudahy TJ, Hewson RD (2008) Mineral mapping for copper porphyry exploration using multispectral satellite and hyperspectral airborne sensors. In: Spencer JE, Titley SR (eds) Ores and orogenesis: circum-pacific tectonics, geologic evolution, and ore deposits, Arizona Geological Society Digest 22. Arizona Geological Society, Tuscon, pp 111–125

Rowan LC, Mars JC (2003) Lithologic mapping in the Mountain Pass, California area using Advanced Spaceborne Thermal Emission and Reflection Radiometer (ASTER) data. Remote Sens Environ 84(3):350–366

Rowan LC, Hook SJ, Abrams MJ, Mars JC (2003) Mapping hydrothermally altered rocks at Cuprite, Nevada, using the Advanced Spaceborne Thermal Emission and Reflection Radiometer (ASTER), a new satellite-imaging system. Econ Geol 98(5):1019–1027

Ruffin C, King RL (1999) The analysis of hyperspectral data using Savitzky-Golay filtering-theoretical basis. 1, Geoscience and remote sensing symposium, 1999. IGARSS '99

proceedings. IEEE 1999 international, Hamburg, Germany vol 2, pp 756–758, 28 Jun–02 Jul 1999. doi:10.1109/IGARSS.1999.774430

Sabine C, Realmuto VJ, Taranik JV (1994) Quantitative estimation of granitoid composition from Thermal Infrared Multispectral Scanner (TIMS) data, Desolation Wilderness, northern Sierra Nevada, California. J Geophys Res 99:4261–4271

Salisbury JW, Walter LS, Vergo N, D'Aria DM (1991) Infrared (2.1-25 mm) spectra of minerals. Johns Hopkins University Press, Baltimore

Salisbury JW, Wald AE, D'Aria DM (1994) Thermal infrared remote sensing of Kirchhoff's Law: 1. Laboratory measurements. J Geophys Res 99(B6):11897–11911

Savitzky A, Golay MJE (1964) Smoothing and differentiation of data by simplified least squares procedures. Anal Chem 36(8):1627–1639

Swayze GA (1997) The hydrothermal and structural history of the Cuprite mining district, southwestern Nevada: an integrated geological and geophysical approach. PhD, University of Colorado, Boulder

Swayze GA, Clark RN, Kruse FA, Sutley SJ (1992) Ground-truthing AVIRIS mineral mapping at Cuprite, Nevada. In: Summaries of the third annual JPL airborne geoscience workshop. R. O. Green. JPL Publication 92–14. Jet Propulsion Laboratory, Pasadena, California, pp 47–49

Tsai F, Philpot W (1998) Derivative analysis of hyperspectral data. Remote Sens Environ 66 (1):41–51

Vaughan RG, Calvin WM (2005) Mapping weathering and alteration minerals in the Comstock and Geiger Grade areas using visible to thermal infrared airborne remote sensing data. In: Rhoden HN, Steininger RC, Vikre PG (eds) Geological Society of Nevada symposium. Geological Society of Nevada, Reno, pp 1–20

Vaughan RG, Calvin WM, Taranik JV (2003) SEBASS hyperspectral thermal infrared data: surface emissivity measurement and mineral mapping. Remote Sens Environ 85(1):48–63

Vaughan RG, Hook SJ, Calvin WM, Taranik JV (2005) Surface mineral mapping at Steamboat Springs, Nevada, USA, with multi-wavelength thermal infrared images. Remote Sens Environ 99(1–2):140–158

Vincent RK, Rowan LC, Gillespie RE, Knapp C (1975) Thermal-infrared spectra and chemical analyses of twenty-six igneous rock samples. Remote Sens Environ 4:199–209

Whitbourn LB, Phillips R, James G, O'Brien MT, Waterworth MD (1990) An airborne multiline CO_2 laser system for remote sensing of minerals. J Mod Opt 37(11):1865–1872

Young SJ, Johnson BR, Hackwell JA (2002) An in-scene method for atmospheric compensation of thermal hyperspectral data. J Geophys Res 107(D24):4774

URL1: http://tes.asu.edu/speclib/index.html

URL2: http://speclib.jpl.nasa.gov

URL3: http://speclab.cr.usgs.gov